Mitigation of radiation damage in macromolecules via tunable ultrafast stroboscopic TEM

Hyeokmin Choe[1,2,3], Ilya Ponomarev[1,3,*], Eric Montgomery[1,3,*], June W. Lau[2], Yimei Zhu[4], Yubin Zhao[3], Ao Liu[3], Alexei Kanareykin[1,3], and Chunguang Jing[1,3,*]

[1]*Euclid Beamlabs LLC, 365 Remington Blvd., Bolingbrook, IL 60440, USA*

[2]*Materials Science and Engineering Division, National Institute of Standards and Technology, Gaithersburg, MD 20899, USA*

[3]*Euclid Techlabs LLC, 365 Remington Blvd., Bolingbrook, IL 60440, USA*

[4]*Department of Condensed Matter Physics and Materials Science, Brookhaven National Laboratory, Upton, NY 11973, USA*

* corresponding authors, email: c.jing@euclidtechlabs.com; e.montgomery@euclidtechlabs.com; ilya.ponomarev@euclidtechlabs.com

Abstract

We report mitigation of electron-beam-induced radiation damage in biological macromolecules using rapid, low-dose transmission electron microscopy (TEM) with a new, tunable, retrofittable stroboscopic pulser. Damage mitigation strategies historically consisted of sample cryoprotection and ultra-low beam current; ultrafast laser-pulsed systems have shown promise, but with day-long acquisition times. We show the first practical, fast, laser-free tunable system, with

acquisition of diffraction series in minutes at 5.2 GHz and 10 pA. This is the largest study to date: two materials ($C_{36}H_{74}$ paraffin and purple membrane), two beam energies (200 keV and 300 keV), two independent microscopes (Schottky and LaB_6), two modes (pulsed and continuous), and unsurpassed repetition rate tunability. Critical dose at room temperature doubled versus continuous beam for ~100 MHz single-electron repetition rates. Results herald a new class of highly-tunable, ultrafast pulsers with future applications in cryogenic electron microscopy (CryoEM), high resolution single particle imaging, and rapid low-dose TEM.

Introduction

Transmission electron microscopy (TEM) and its suite of analytical approaches provides unparalleled spatial resolution for characterization of material morphology, structure, and chemistry from sub-nanometer to micrometer scales. But the hundreds of keV electron beam causes resolution-limiting radiation damage, especially for sensitive crystal structures such as organic and biological macromolecules, due to elastic and inelastic scattering in the sample [1,2]. Elastic scattering of the electron beam with the sample nuclei can result in atomic displacement or ejection of atoms. Inelastic scattering from electron-electron interactions can cause ionization damage (radiolysis). Both scattering processes contribute to electrostatic charging, hydrocarbon contamination and heating of the sample [3–5]. Radiolysis is particularly deleterious to crystal structure, degrading diffracted intensities during beam exposure [3,6].

A critical dose is defined as the threshold at which the maximum intensity of particular diffraction spots or rings drops to $1/e$ of its original value [7,8]. Critical dose limits the resolution of images, diffraction patterns, and electron tomography [9]. Among numerous strategies to reduce electron beam damage, cryoprotection [10–13] has been highly effective for biological specimens. Until recently, critical dose has been considered independent of dose rate. However, several groups have recently reported mitigation of radiation damage via ultrafast electron pulses [14–17]. To date, studies have used either femtosecond laser-driven ultrafast electron pulses with kHz to MHz repetition rate, or a pulsed beam of fixed frequency produced by radiofrequency (RF) deflecting cavities. An in-depth study of a tunable GHz pulse structure and its impact on critical dose is intractable with these approaches. Additionally, rigorous comparison of pulsed and

continuous beam on the same microscope has been challenging on the femtosecond scale, because the laser-driven cathode modifications replace the normal thermionic or Schottky field emission cathode used for (continuous) operation of the TEM [18], and photoemission beam size, divergence, and energy spread differ from thermionic or Schottky emission on the same cathode.

We report for the first time rigorous evidence for radiation damage mitigation via tunable, periodically-gated beams in two independently modified stroboscopic TEMs, directly compared to normal continuous beam in the same TEM. A new technology for pulsed beam generation enables this result; the Euclid STROBO-X00 series allows push-button on/off control of pulsed mode using the original cathode. Both 300 keV thermionic and 200 keV Schottky-emission beam sources show consistent results. Using two model macromolecules, $C_{36}H_{74}$ paraffin and purple membrane (bacteriorhodopsin), we calculated a critical dose from a time-intensity diffraction series (fading curves) in selected-area diffraction mode. We show clear improvement in damage mitigation in single-electron-packet mode when an equivalent dose is delivered with a periodic tunable-width picosecond gate regulating single-electron arrival at the specimen. Critical dose for pulsed beam was improved by a factor of up to 2 at room temperature compared with the continuous random beam while keeping constant the total accumulated dose, beam optics, and illuminated sample area. This factor of 2 exceeds femtosecond laser-based mitigation efforts recently reported at 200 kHz in paraffin [14], but is achieved at a remarkable 100 MHz average single-electron repetition rate for both model macromolecules, leading to orders of magnitude faster data acquisition on a highly tunable system.

Results

Tunable gating for single-electron arrival or pulsed beam with STROBO-X00 series

Results were acquired using a new highly tunable beam pulser. Fig 1a illustrates a pulsed electron beam generated by the Euclid Techlabs beam pulser [19,20]: a STROBO-200 on a JEOL JEM-2010F at Brookhaven National Laboratory (BNL), and a STROBO-300 on a JEOL JEM-3010 at the National Institute of Standards and Technology (NIST) [21].

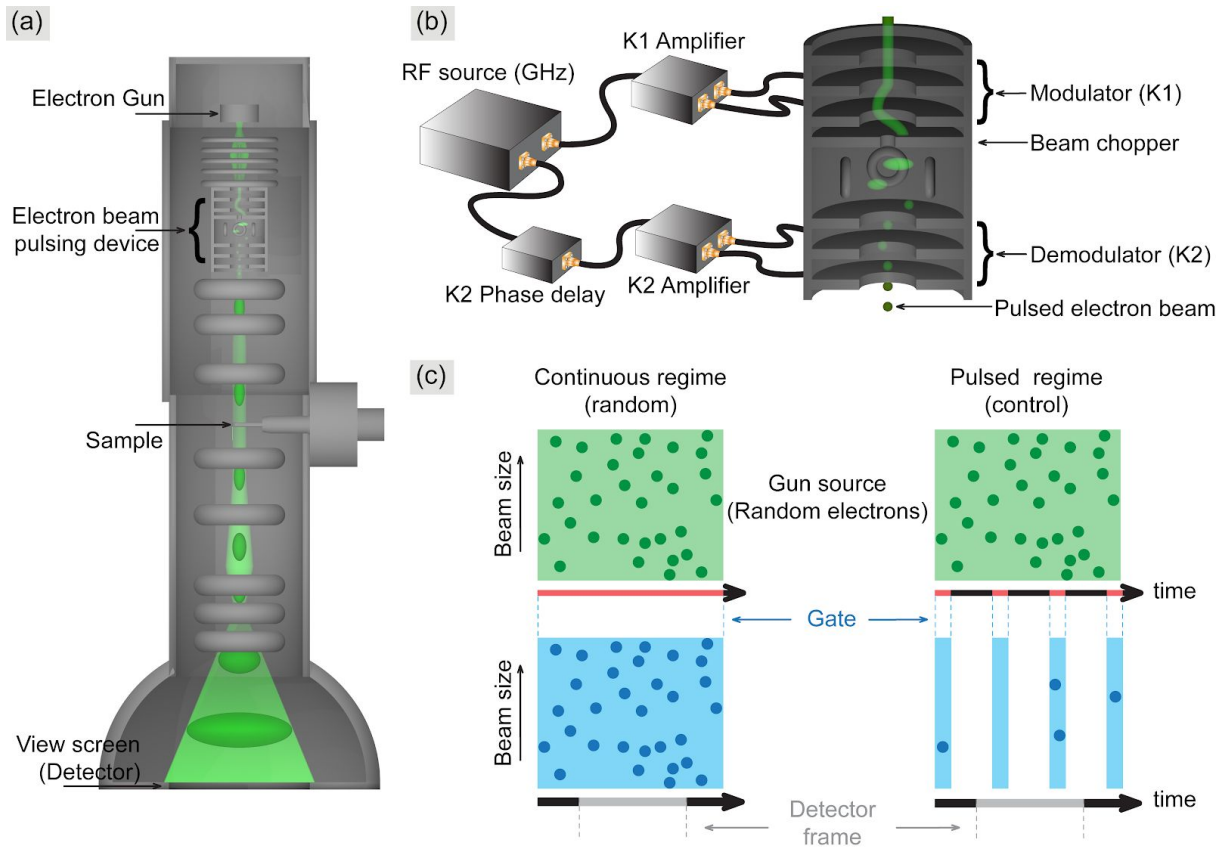

Figure 1. (a) STROBO-X00 series GHz stroboscopic TEM system. (b) 40 MHz - 6 GHz RF feeds K1 (and K2 with 180º phase delay) to sweep beam across the chopper aperture, then demodulate sinusoidal transverse momentum. (c) Adapted from [14]. Beam has two modes, continuous, or pulsed, where electrons are gated as shown. Gate width and frequency are tunable. The detector frame (the time to acquire a single diffraction pattern) averages across millions of gate periods (not to scale).

Although the gating frequency was fixed in this paper (5.2 GHz), the STROBO-X00 is a broadband device that can, in principle, smoothly tune stroboscopic pulse trains from 80 MHz to 12 GHz. This capability enables custom tailoring the time-structure of the beam to match periodic dynamic processes in many classes of materials. A unique traveling wave stripline architecture overcomes the narrow frequency band limitations of RF resonator cavity deflectors.

Direct comparison of critical dose between pulsed and continuous beams using the microscope's native beam emission process (LaB_6 filament at NIST, Schottky at BNL) is rather straightforward - in contrast to laser-based modified cathodes where pulsed beam requires switching to photoemission and continuous beam may not even be an option. Enabling

continuous beam (native TEM functionality) in the STROBO-X00 series is as easy as toggling off RF power to the modulator (K1) and demodulator (K2) (Fig. 1b and 1c). Pulsed beam is produced by modulating the beam using K1 to produce a transverse sinusoidal RF field. The modulated beam, still continuous as it exits K1, is swept across a 0.025 mm diameter chopping aperture. The beam is now gated as it exits the beam chopping aperture, and it is demodulated by K2 to cancel the transverse momentum introduced by K1. Beam into the pulser was reduced to tens of pA (single-electron regime), where most windows (Fig. 1c) do not have a random electron, but those that do are highly likely to have only a single electron. Each electron in the resulting pulse train is now separated in time from the next electron by at least the gating period. We varied the gate duration in this work (by increasing RF power in K1) while holding the gate period constant, and measured average electron arrival rates from 72 - 624 MHz (Table 2). The single-electron packet regime is well-controlled with a short gate width while still achieving high average electron arrival rate (72 MHz at 10% duty cycle) and hence rapid diffraction pattern acquisition. Experiments were calibrated in the "continuous random" regime, i.e. normal TEM beam to quantify the critical dose of the beam-sensitive materials in standard experimental conditions. Then we tested "pulsed random" effects by varying duty cycle (i.e., gate width) while holding the accumulated dose and illuminated area constant, for paraffin and purple membrane, on the two standalone STROBO-X00 systems.

Calibrating radiation damage in organic $C_{36}H_{74}$ paraffin crystal with continuous beam

Figure 2a shows a typical diffraction pattern obtained from a $C_{36}H_{74}$ paraffin crystal under “continuous random” electron beam using 300 keV TEM, before (top) and after (bottom) exposure to a standard dose of 0.1 e^-/nm^2 (10 $e^-/Å^2$) at room temperature. Diffraction patterns were obtained with 19.39 pA averaged continuous beam current, and the illuminated area was 21.2 μm^2. In Figure 2b, the fading curve data were calculated from the series of diffraction patterns shown in Figure 2a. The grey line is the critical dose (D_{cri}), defined as the accumulated electron dose at which the relative intensity (I / I_0) of the selected diffraction peak decreases to $1/e$ (~37%).

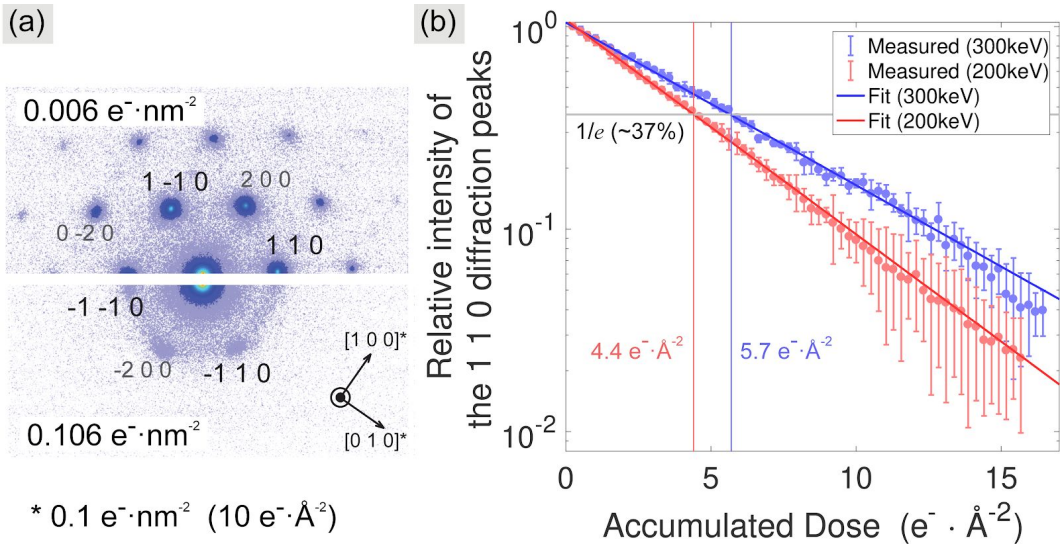

Figure 2. (a) Single crystal electron diffraction on the indexed [001] crystallographic zone-axis for orthorhombic $C_{36}H_{74}$ paraffin crystal (a = 7.4 Å, b = 5.0 Å) [22] at room temperature, before and after exposure to 0.1 e^-/nm^2 (10 $e^-/Å^2$) in a 300 keV TEM with a camera length of 300 mm. (b) Fading of the 110 family reflections versus total accumulated electron dose are shown for 200 keV (lower, red) and 300 keV (upper, blue), critical dose (D_{cri}) in grey. Error bars are standard deviation over 10 measurements on separately prepared samples.

Since dynamic scattering effects are negligible, the Bragg peak intensity decay as a function of the accumulated total dose is evidence of increasing crystal disorder and irreversible structural damage [5,7,22]. To study the effect of electron kinetic energy, dose series were acquired at two different energies: 200 keV and 300 keV. At 300 keV, we observed slower decrease in the relative intensity of the $C_{36}H_{74}$ paraffin 110 diffraction peaks, shown in Figure 2b, possibly because the inelastic scattering cross-section is 1.13 times larger at 200 keV than at 300 keV [13]. We estimate that the D_{cri} for $C_{36}H_{74}$ paraffin in the 300 keV TEM is approximately 0.057-0.061 e^-/nm^2 (5.7−6.1 $e^-/Å^2$), as calculated from an exponential fit to the upper curve in Fig. 2b. Likewise, D_{cri} for $C_{36}H_{74}$ paraffin in the 200 keV TEM was about 0.044 e^-/nm^2 (4.4 $e^-/Å^2$), shown in Fig. 2b, lower curve. The results are comparable to D_{cri} of 0.034-0.038 e^-/nm^2 (3.4−3.8 $e^-/Å^2$) reported for $C_{36}H_{74}$ paraffin in a 100 keV electron microscope [13,23,24], and 0.044-0.055 e^-/nm^2 (4.4−5.5 $e^-/Å^2$) for 200 keV [14].

Mitigation of paraffin radiation damage by tunable pulsed beam

Pulsed beam mode diffraction series showed significant mitigation of $C_{36}H_{74}$ paraffin radiation damage. We discuss 300 keV results here and include the same experiment repeated at 200 keV. We first used electron pulses with a 22% duty cycle factor at 5.2 GHz repetition rate, i.e. 43 ps pulse length and 192 ps period. Total accumulated critical dose (D_{cri}), beam optics, and illuminated sample area were the same as for the continuous beam (Table 2). Figure 3a compares the continuous- and pulsed-beam induced radiation damage. The diffraction patterns were taken with 0.002546 e^-/nm^2/frame (0.2546 $e^-/Å^2$/frame) electron dose rate on the specimen (0.5 second detector exposure) so that the averaged total beam current and illuminated areas for the pulsed mode were kept as 100.1±0.38 pA and 122.7±0.11 μm^2, respectively. Paraffin crystal sizes were about 1200 μm^2, so each pattern was obtained from a single crystal. The higher-order reflections are clearly visible in Figure 3a after dosing with the pulsed electron beam compared to those with the continuous beam at the same total accumulated dose 0.060 e^-/nm^2 (6.0 $e^-/Å^2$), suggesting the pulsed electron beam has a lower rate of radiation damage for the $C_{36}H_{74}$ orthorhombic crystal structure. In order to confirm this result, the decrease in relative intensity of the 110 family Bragg reflections (i.e., fading curve) was acquired for two different duty cycles at the same 5.2 GHz repetition rate. In Figure 3b, the fading curves are shown for the 110 family Bragg peak intensities (circled spots on Figure 2a) from paraffin two-dimensional single crystals under continuous (100%, blue dots) and pulsed (22%, pink dots) beam. The critical dose was obtained by an exponential decay fit of the fading curves. Table 1 shows that the critical dose using 300 keV varies between 0.0571 and 0.1124 e^-/nm^2 (5.71 and 11.24 $e^-/Å^2$), for 100% and 10% duty cycles, respectively. This factor of 2 improvement is comparable to the 1.8x dose rate improvement in the paraffin fading curve reported by University of Minnesota for 200 keV femtosecond laser-generated single-electron packets [14].

While achieving similar results, the STROBO-X00 series pulser enabled much higher repetition rate than laser-based pulsed TEM, and thus fast image acquisition. For comparison, laser-based pulsed TEM is typically operated at <0.1GHz [20], and in the Minnesota study was

limited to 200 kHz single-electron pulse trains which took 22 hours to acquire 2% of the fading curve [14]. For comparable illuminated area we achieved an effective time-averaged arrival rate of 73 MHz or higher for single-electron packets (see Table 2), 0.5 s acquisition time per frame, and just minutes to acquire a full pulsed-beam fading curve.

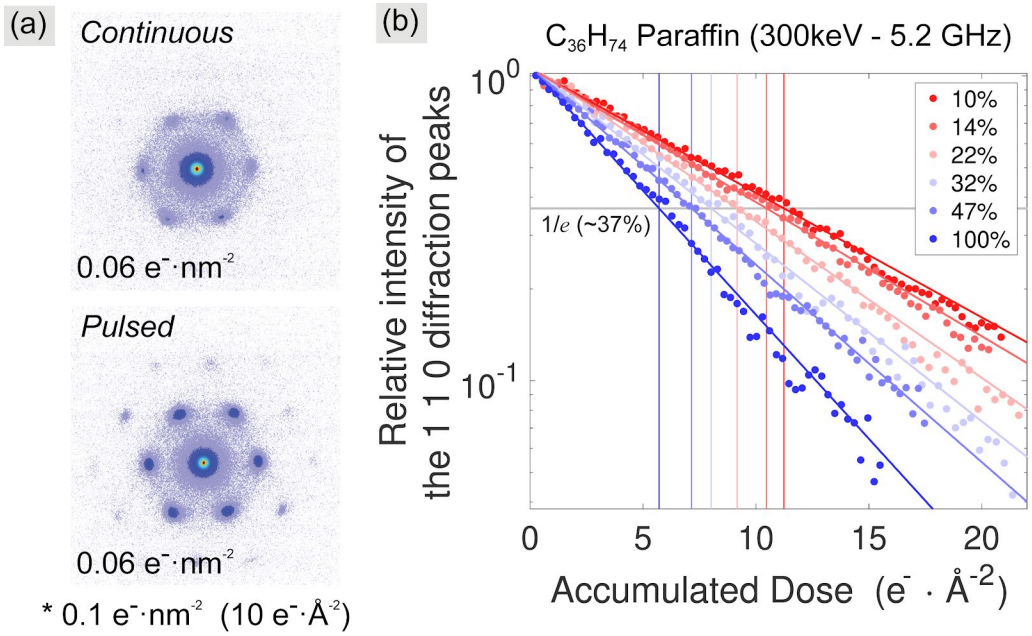

Figure 3. Mitigation of radiation damage at different duty factors of pulsed electrons. (a) Selected continuous- and pulsed-beam diffraction patterns of a paraffin crystal with the 110 family Bragg peaks highlighted. (b) Fading curves from the 110 family reflections and exponential decay fits as a function of pulsed beam duty cycle factor at 5.2 GHz repetition rate for the same dose rate (0.2546 $e^-/Å^2$/frame), grey guideline indicating critical dose (D_{cri}).

Unlike resonator-based approaches [17], the method used in this study is continuously tunable (in principle from low frequency to ~12 GHz) for mitigation of critical dose and minimization of acquisition time using pulse structures tailored to individual material properties.

Euclid Techlabs LLC's STROBO-300 system installed at NIST provides a 300 keV tunable length electron pulse, corresponding to different duty cycles in Figure 3, by varying the RF power fed to the beam pulser (see also Figure 1b). The tunable duty cycle enables precise gating of the statistical arrival distribution of electrons on the specimen, and in combination with low beam current allows single electron packets with controllable average arrival time separation

on the sample. Figure 3b shows the relative intensity of the 110 diffraction peaks fading curves as a function of six different duty cycle settings (i.e., six different RF power levels to K1). Intensities were monitored until all diffraction peaks in the pattern had faded. The duty cycle-dependences of the critical dose presented in Table 1 were calculated by exponential decay fits. The observed critical dose (D_{cri}) strongly improves when the gating time-window is shortened, thereby reducing average electron arrival rate. Here, the 10% duty cycle at 5.2 GHz repetition rate improves the critical dose up to a factor of 2 at room temperature compared to continuous beam.

Mitigation of purple membrane radiation damage by tunable pulsed beam

As a complement to the paraffin studies, we also studied radiation damage mitigation for a purple membrane by capturing powder diffraction patterns at regular time intervals (see Table 2) until diffraction patterns had faded. Electron powder diffraction patterns were taken from large areas containing many small (~1μm^2) particles of purple membrane at room temperature, and show powder diffraction rings characteristic of a circularly averaged hexagonal lattice with p3 symmetry (a = 62 Å) [25–27]. The series of diffraction patterns were analyzed by measuring the intensity for the (430) powder diffraction rings (d-spacing = 8.827 Å) [25] at each time interval and relating that the total accumulated electron dose at that time. The signal intensities were normalized to their initial highest intensity and followed as a function of accumulated total electron dose.

Figure 4a shows that the pulsed beam reduced radiation damage to the purple membrane: the (430) diffraction intensity at the same total accumulated dose 0.014 e^-/nm^2 (1.4 $e^-/Å^2$) is stronger after exposure with a pulsed beam compared with a continous beam. Figure 4b shows the relative intensity of the (430) diffraction ring fading curves as a function of different duty cycles. Just as with paraffin, the critical dose (grey guideline) of the fading curves improves when the pulse length is shortened (Table 1). The exponential decay fit provides a cut-off critical dose of the fading curve at 1/*e* so it can be analyzed by the duty cycle dependent improvement factor. Here, the 10% duty cycle at 5.2 GHz repetition rate improves the critical dose up to a

factor of 2.1 at room temperature, similar to the paraffin, indicating that tuning the electron arrival rate is an effective mitigation strategy for radiation damage in both biological specimens.

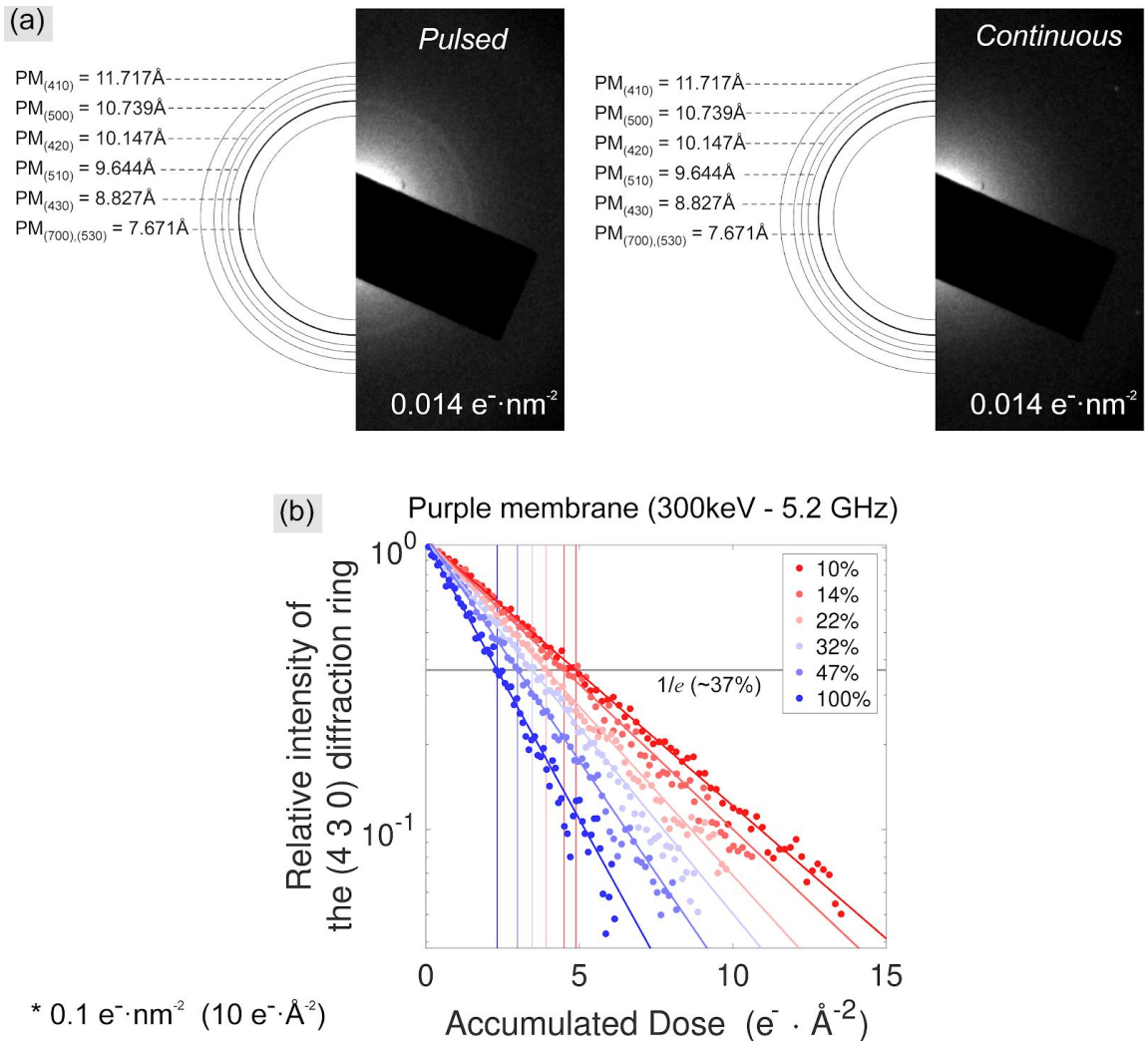

Figure 4. Comparison of the continuous random and pulsed random electron beam damage for the same dose rate (0.1045 $e^-/Å^2$/frame). (a) Selected continuous- and pulsed-beam powder diffraction patterns of a purple membrane with the (430) rings at total accumulated dose 0.014 e^-/nm^2 (1.4 $e^-/Å^2$). Rings are diffuse, possibly due to sample thickness or vibrational blurring from soft phonon modes at room temperature. (b) Fading curves from the (430) powder rings and non-linear exponential decay fits for each measured duty cycle factor from 10 to 100%.

Energy dependence of radiation damage for both macromolecules using pulsed mode

Figure 5 compares the 10% duty factor pulsed mode fading curves of the relative intensity for both (a) organic $C_{36}H_{74}$ paraffin 110 diffraction peaks and (b) purple membrane

(430) ring at 300 keV and 200 keV. For comparison at two electron energies under pulsed mode, we performed the experiments at the NIST (300 keV) and BNL (200 keV) microscopes in exactly the same way using the same specimen on the same grid with the same pulsed mode conditions, 5.2 GHz repetition rate and 10% duty cycle factor. At each microscope, we simply moved onto a fresh single-crystal region on that same specimen. We show in Table 1 the critical doses (D_{cri}), defined as the total accumulated electron dose (1 e^-/nm^2 = 100 $e^-/Å^2$) at which the selected relative intensities is reduced to 1/*e* of their initial value.

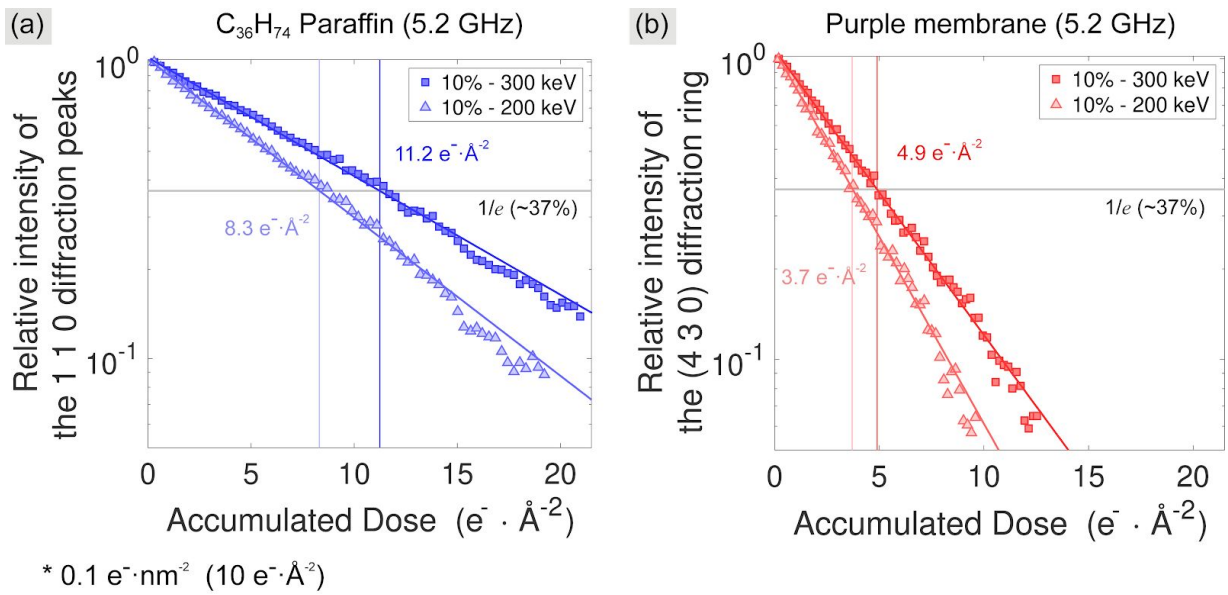

Figure 5. Comparison of electron radiation damage for 200 keV and 300 keV TEM in pulsed mode at 10% duty factor for both (a) organic $C_{36}H_{74}$ paraffin and (b) macromolecular purple membrane. An energy-dependent slope is partially attributable to 1.13x higher inelastic scattering for carbon at 200 keV versus 300 keV [13] which, despite equal dose rates, causes lower electron-specimen interaction rates at 300 keV. Although purple membrane is more damage-sensitive from the point of view of the critical dose, the mitigative effect of a 5.2 GHz 10% duty beam is also~2x, like the paraffin sample (see Table 1), hinting at a common damage mechanism mitigated by pulsed beam in both organic macromolecules.

We estimate D_{cri} from the exponential decay fit as the dose at 1/*e* of the initial intensity. The critical dose for $C_{36}H_{74}$ paraffin at 300 keV with 10% duty cycle pulsed mode is determined to be ~ 0.112 e^-/nm^2 (11.2 $e^-/Å^2$). The paraffin critical dose is on average 1.35±0.6 times higher at 300 keV than at 200 keV. Similarly, purple membrane shows an improvement factor of about

1.31±0.18 at 300 keV compared to 200 keV. Critical dose in both biomolecules exhibits a similar energy dependence under pulsed mode electron beam. Our measured critical dose improvements agree within the margin of error with the energy dependence reported for the carbon inelastic scattering cross-section: 1.13 times larger at 200 keV than at 300 keV [13], compared to critical dose 1.35±0.6 and 1.31±0.18 times larger for paraffin and purple membrane, respectively. Full results of the energy dependence of critical dose under pulsed mode, spanning duty cycles from 10−100%, are shown in Table 1.

Sample	***Duty Cycles (D_f) @ 5.2 GHz*** ***Electron Energy***	***100% (cont. mode)***	***47%***	***32%***	***22%***	***14%***	***10%***
$C_{36}H_{74}$ paraffin	***300 keV***	5.71±0.43	7.15±0.46	8.02±0.56	9.17±0.7	10.47±0.57	11.24±0.9
	200 keV	4.41±0.29	5.43±0.49	6.02±0.45	6.83±0.54	7.79±0.57	8.31±0.32
	Ratio 1 (300 keV/200 keV)	1.3±0.36	1.32±0.48	1.33±0.51	1.34±0.62	1.34±0.57	1.35 ±0.6
	Ratio 2 [200 keV] (D_f / cont.)	1	1.23±0.39	1.37±0.37	1.55±0.42	1.77±0.43	1.88±0.31
	Ratio 3 [300 keV] (D_f / cont.)	1	1.25±0.46	1.4±0.49	1.6±0.56	1.83±0.5	1.97±0.66
Purple membrane	***300 keV***	2.32±0.21	2.98±0.2	3.46±0.27	3.92±0.25	4.5±0.34	4.89±0.24
	200 keV	1.81±0.09	2.32±0.08	2.68±0.15	3.02±0.22	3.52±0.19	3.73±0.11
	Ratio 1 (300 keV/200 keV)	1.28±0.15	1.29±0.14	1.29±0.21	1.3±0.24	1.28±0.26	1.31±0.18
	Ratio 2 [200 keV] (D_f / cont.)	1	1.28±0.09	1.48±0.12	1.67±0.16	1.94±0.14	2.06±0.1
	Ratio 3 [300 keV] (D_f / cont.)	1	1.29±0.21	1.49±0.24	1.69±0.23	1.94±0.28	2.11±0.23

Table 1. Critical doses (1 e^-/nm^2 = 100 $e^-/Å^2$) of $C_{36}H_{74}$ paraffin 110 family reflections, and purple membrane (430) ring, measured by intensity fading to 1/*e* for different duty cycles (%) at 5.2 GHz repetition rate from an exponential decay fit. Ratio 2 and 3 are the average of 200 and 300 keV results, respectively.

Discussion

For both $C_{36}H_{74}$ paraffin and purple membrane (bacteriorhodopsin) organic macromolecules, at room temperature, a comparison of continuous and pulsed electron beam via analysis of the fading curves of electron diffraction patterns (i.e. single crystal diffraction spots and powder rings) shows remarkable, repeatable damage mitigation in macromolecules by tuning the width of the periodic gate for single-electron arrival at the sample. Results are consistent between independent microscopes and comparable at 300 and 200 keV, given the beam energy dependence of inelastic scattering cross-section. It is now possible to mitigate beam-induced radiation damage in biomedical materials using tunable stroboscopic GHz-gated electron beam. Image acquisition time using a GHz pulser is orders of magnitude faster than that for systems with hundreds-kHz repetition rate limited by laser pulse frequency, yet achieves comparable or higher improvements in critical dose by accessing the same statistical single-electron packet regime. These studies strongly point to future opportunities for ultra low-dose as well as pump-probe macromolecular dynamics experiments using tunable picosecond pulsed electron beams.

Pulse structure analysis

Until now, technological barriers have limited this type of repetition rate and pulse-width dose analysis. Here we analyze over a wide range of average single-electron repetition rates (~60 - 600 MHz) the effect on the critical dose. We model our continuous random beam with a Poisson distribution in Figure 6a, showing the single-electron-per-pulse approximation holds. Each dot represents the modeled two-electron arrival probability within a single gate width versus calculated average arrival frequency for each experimental duty factor (Table 2). The approximation of one electron per packet is good to 0.1%. In Figure 6b we plot paraffin and purple membrane critical dose improvement over continuous random beam (from fits in Figures 3b and 4b) versus the average arrival frequency of single electrons. Each data point represents a different duty cycle factor at 300 keV. Improvements are most obvious in the <100 MHz range, consistent with attributions of critical dose improvements in the pulsed single-electron-packet

regime to acoustic phonon dissipation within the sample [17] or local heating effects on radical diffusion [14]. Moreover, we suggest that the observed sample-specific improvement merits study into an optimum pulse structure varying by material. For a given macromolecule, then, stroboscopic TEM acquisition time may be shortened while preserving any imaging benefits of improved critical dose simply by tuning beam current, pulsed TEM frequency, and gate width to an optimum tailored to the given sample material.

Figure 6 makes plain that the statistical nature of the electron emission process (whether photo-, thermionic, or field emission) leads to substantially non-zero probabilities of multiple electron arrivals in short periods of time. Pulsing or gating is simply a means of restricting the allowed arrival frequencies to make single-electron packets more likely, albeit not guaranteed.

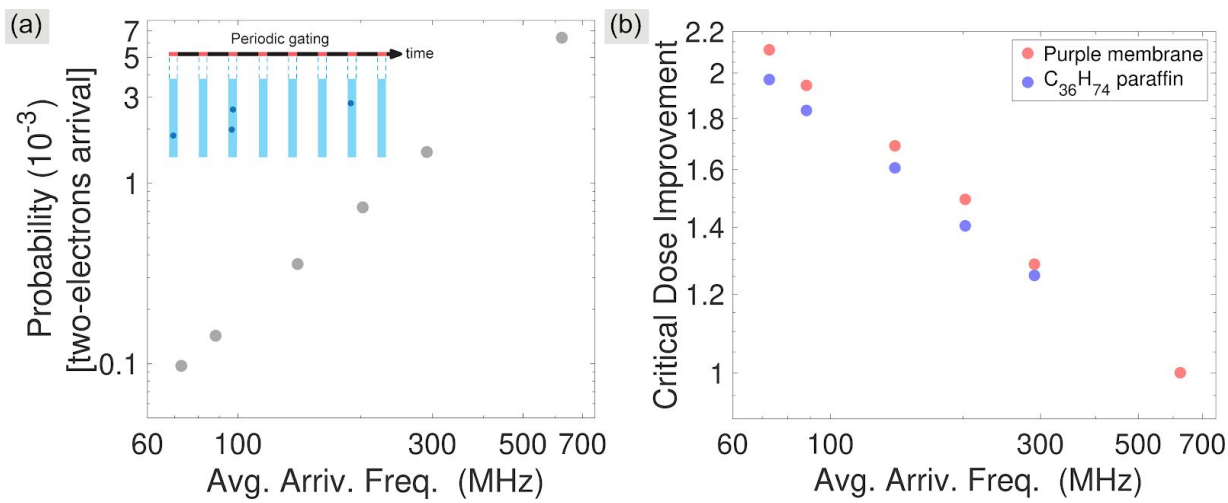

Figure 6. (a) Statistical model of electrons per gate at low current, as the Poisson probability of finding two random electrons in the same gate, $p_2 = \frac{N_{avg}^2}{2!} \cdot exp(-N_{avg})$, where p_2 is the probability of arrival of 2 electrons given average electrons per window N_{avg}. Probability is plotted versus average arrival frequency, which is calculated by multiplying the repetition rate with the average number of electrons per gate at a given current and duty cycle. (b) The measured critical dose improvement (Ratio 3 in Table 1) versus average arrival frequencies for both organic $C_{36}H_{74}$ paraffin and purple membrane using 300 keV stroboscopic TEM.

Double-electron arrival is a necessary but not sufficient condition for double interaction. In Figure 6, while the probability of multiple electrons arriving at the sample within a gating period appears inversely correlated with critical dose improvements, the magnitude of that

probability is not strictly correct for damage rate discussions. Most electrons arriving at the sample do not interact and scatter. So for gates with 2 or more electrons arriving, usually a single electron will scatter or none at all. The question is then how many gates have 2 electrons not merely arriving, but interacting with the sample, in a given diffraction pattern acquisition time. Using our 0.5 seconds for acquisition at 5.2 GHz and 10 pA, we have 2.6 billion gates integrated to obtain that image. For 10% duty factor, 0.01% of the gates have two electrons as in Figure 6, and assuming scattering rates of 5e-6 (for carbon, ~2e-7 inelastic, ~5e-6 elastic near 200-300 keV [13]) where both electrons must scatter independently, this yields an average of (2.6 billion x 0.01% x $(5e\text{-}6)^2$) or 0.065 double-scattering gates per million diffraction images taken. Double-scattering within a single gate is negligible even on imaging timescales.

A related question respects the delay time between electron arrival events. Presumably a threshold delay is required in order to achieve critical dose improvements above 2. For the periodic gating at 5.2 GHz and 10% duty cycle presented in this work, pulses can arrive within one gate (arriving within 19.2 ps) or within adjacent gates (arriving with spacing 172.8 - 211.2 ps). Applying the same reasoning as before regarding scattering rates, most electrons arriving in rapid succession will not interact with the sample. Average interaction frequency will be proportional to the average arrival frequency times the scattering rate. That figure, for our 10% duty cycle, 72 MHz arrival frequency case, is about 360 elastic and 14 inelastic interactions per second. Such low rates imply complete thermalization and cooling of the sample after each event. They also suggest there may be room to increase beam current and tune repetition rates still higher; we note gating at 5.2 GHz was studied here but the STROBO-300 system is capable of 12 GHz as designed.

The statistical chance of multiple electrons per pulse is important, but so too is the practical time required to obtain images. This reinforces a key advantage of our approach: the multi-electron probability can be kept as low as with laser-based systems, but our repetition rate is perhaps a thousand times higher while maintaining tunability. Thus images are acquired in a fraction of the time, TEM system stability and drift are much less critical, and the productivity of a machine retrofitted with a GHz pulser rather than a laser is much preferable when doing low-dose imaging.

Potential benefits of tunable pulsed CryoEM

All experiments presented here were performed at room temperature. We specifically highlight the 10 nanosecond (100 MHz) timescale which was found to correspond to doubling of critical dose: a major question is whether even higher critical dose may be possible, for instance in cryogenic conditions. If indeed a significant contributing factor to damage mitigation is phonon damping following single-electron interaction, or radical diffusion from local heating, this provides strong motivation for incorporating tunable GHz pulser technology into a cryogenic electron microscope (CryoEM). Faster damping or cooling of the sample than at room temperature might permit higher repetition rates, faster acquisition, and perhaps even higher critical dose. Material-dependent pulse optimization could be studied. In particular, the impact of pulsed beam irradiation on recrystallization of low density amorphous (LDA) water into ice, a perennial impediment to CryoEM imaging, would be of high interest. And for single-particle imaging, increased critical dose could enable higher resolution structural determination.

Methods

Sample preparation

Two model biological macromolecular specimens were used in this study. The organic material is $C_{36}H_{74}$ paraffin, which forms thin, orthorhombic single crystals oriented along the [001] crystallographic direction upon drop-casting from solution onto a substrate. The paraffin solution was prepared by dissolving $C_{36}H_{74}$ paraffin powder (98% purity n-hexatriacontane, Sigma-Aldrich) in n-hexane solvent (95% purity, Consolidated Chemical & Solvents LLC). Samples for use in TEM were prepared by pipetting a droplet of the $C_{36}H_{74}$ paraffin solution onto carbon coated copper (Cu) TEM grids (SPI Supplies) followed by solvent evaporation in air.

Purple membrane was isolated from H. salinarum strain S9 by the standard method [28] and diluted to 3 mg/ml in 0.1 M potassium phosphate buffer at pH 5.2 [29]. All the samples were provided by Drs. Joseph Mckeown and Megan Shelby (Lawrence Livermore National Laboratory). The purple membrane solution was washed by pelleting via centrifugation at 12000

rpm for 1.5 hours until the supernatant was clear and then resuspended in water. The sample was deposited onto a carbon-coated Cu mesh by dropping 2 µl of 2 mg/ml in 2% glucose in water onto the grid and allowing the solution to fully air dry without blotting.

STROBO-X00 operation and electron diffraction via picosecond electron pulses

Electron crystallography experiments were performed at two stroboscopic TEM facilities to ensure repeatability: a modified 300 keV LaB_6-based thermionic TEM (JEM-3010, JEOL, with a Euclid STROBO-300) and a modified 200 keV Schottky-emission TEM (JEM-2010F, JEOL, with a Euclid STROBO-200). 5.2 GHz chopping duty cycle factors were calibrated for each machine using a Faraday cup and a 6517B Keithley picoammeter. By using a GHz radio-frequency (RF) microwave source to precisely control the electron chopping process, electron packets as short as twenty picoseconds in duration are delivered to the specimen at tunable GHz repetition rates; here the electron beam current was reduced to tens of pA (single-electron-packet regime) and so the pulse width is less meaningful than the single electron arrival rate (Table 2).

All diffraction patterns were recorded by Gatan Orius SC1000 CCD camera at room temperature, using an indicated camera length of 300 mm. The electron beam current in the single-electron-packet regime was between 10 and 100 pA and the illuminated area approximately 5−18 µm in diameter (measured accurately using a cross grating replica for calibration of magnification), with illuminated area standardized across dose series (Table 2). For $C_{36}H_{74}$ paraffin, a series of 54−70 frames × 0.5 s exposures was acquired at a flux of 0.2564 $e^-/Å^2$/frame. Beam-induced damage was studied by locating a fresh area of paraffin crystal in bright field mode followed by capture of diffraction patterns at set time intervals until diffraction peaks had faded [14,30]. The series of diffraction patterns were analyzed by measuring the intensity of pairs of Bragg peaks (typically the {110} family: marked circles on Figure 4a) at each time interval and relating that to the accumulated electron dose up to that time. Intensities were averaged and normalized against the initial highest intensity. The accumulated electron dose (D_{accum}) is determined as $D_{accum} = \frac{I \cdot t}{A}$, where I is beam current ($e \cdot s^{-1}$), t is the exposure time (s), and A is the illuminated beam area ($Å^{-2}$).

For purple membrane, a series of 64 frames × 0.5 s exposures at a flux of 0.001045 e^-/nm^2/frame (0.1045 $e^-/Å^2$/frame) was acquired. Electron diffraction rings of purple membrane were analyzed by a radial averaging method [13,29,31], then the average intensities in one resolution zone (centered at 9 Å) were normalized to their initial intensity and followed as a function of accumulated electron dose. Gatan DigitalMicrograph and MATLAB software were used for image capture and analysis, respectively. Beam is on the cathode during detector readout, but readout in microseconds is a negligible fraction of the acquisition time per frame (0.5 s). All the experimental parameters discussed in this report are summarized in Table 2.

Sample	***Beam type***	***Freq. (GHz)***	***Duty cycle (%)***	***Avg. beam current (pA)***	***Average electrons / pulse***	***Avg. arriv. freq. (MHz)***	***Beam area (μm^2)***	***Acq. time (s)***	***Frame Interval time (s)***	***Total acquired images (frames)***
Paraffin ($C_{36}H_{74}$)	Contin.	N/A	N/A	19.39	N/A	N/A	21.24	0.5	4.5	65
	Contin.	5.2	100	100.13	0.12	624	122.72	0.5	5	54
	Pulsed	5.2	47	46.78	0.056	291.2	122.34	0.5	10.7	64
	Pulsed	5.2	32	32.53	0.039	202.8	122.85	0.5	15.4	59
	Pulsed	5.2	22	22.14	0.027	140.4	122.18	0.5	22.6	60
	Pulsed	5.2	14	14.36	0.017	88.4	122.39	0.5	34.9	65
	Pulsed	5.2	10	10.38	0.014	72.8	122.76	0.5	48.2	70
Purple membrane	Contin.	5.2	100	100.04	0.12	624	298.65	0.5	5	64
	Pulsed	5.2	47	47.12	0.056	291.2	298.48	0.5	10.6	64
	Pulsed	5.2	32	32.62	0.039	202.8	298.78	0.5	15.3	68
	Pulsed	5.2	22	21.97	0.027	140.4	298.13	0.5	22.8	68
	Pulsed	5.2	14	14.11	0.017	88.4	298.25	0.5	35.4	73
	Pulsed	5.2	10	10.13	0.014	72.8	298.06	0.5	49.4	73

Table 2. Summarized experimental parameters.

Data Availability

All the data that support the findings of this study are available within the paper or from the corresponding author upon reasonable request.

References

1. Egerton, R. F. Control of radiation damage in the TEM. *Ultramicroscopy* vol. 127 100–108 (2013).
2. Jiang, N. Electron beam damage in oxides: a review. *Rep. Prog. Phys.* **79**, 016501 (2016).
3. Egerton, R. F., Li, P. & Malac, M. Radiation damage in the TEM and SEM. *Micron* **35**, 399–409 (2004).
4. S'ari, M., Cattle, J., Hondow, N., Brydson, R. & Brown, A. Low dose scanning transmission electron microscopy of organic crystals by scanning moiré fringes. *Micron* **120**, 1–9 (2019).
5. Chen, Q. *et al.* Imaging Beam-Sensitive Materials by Electron Microscopy. *Adv. Mater.* e1907619 (2020).
6. S'ari, M. *et al.* Analysis of Electron Beam Damage of Crystalline Pharmaceutical Materials by Transmission Electron Microscopy. *J. Phys. Conf. Ser.* **644**, 012038 (2015).
7. Henderson, R. & Glaeser, R. M. Quantitative analysis of image contrast in electron micrographs of beam-sensitive crystals. *Ultramicroscopy* vol. 16 139–150 (1985).
8. Ohno, T. Fading and broadening of electron diffraction spot from beam‐damaged multiple monolayer films. *J. Microsc.* **184**, 17–21 (1996).
9. Aronova, M. A., Sousa, A. A., Zhang, G. & Leapman, R. D. Limitations of beam damage in

electron spectroscopic tomography of embedded cells. *J. Microsc.* **239**, 223–232 (2010).

10. Evans, J. E. *et al.* Low-dose aberration corrected cryo-electron microscopy of organic specimens. *Ultramicroscopy* **108**, 1636–1644 (2008).
11. Karuppasamy, M., Karimi Nejadasl, F., Vulovic, M., Koster, A. J. & Ravelli, R. B. G. Radiation damage in single-particle cryo-electron microscopy: effects of dose and dose rate. *J. Synchrotron Radiat.* **18**, 398–412 (2011).
12. Vinothkumar, K. R. & Henderson, R. Single particle electron cryomicroscopy: trends, issues and future perspective. *Q. Rev. Biophys.* **49**, e13 (2016).
13. Peet, M. J., Henderson, R. & Russo, C. J. The energy dependence of contrast and damage in electron cryomicroscopy of biological molecules. *Ultramicroscopy* **203**, 125–131 (2019).
14. VandenBussche, E. J. & Flannigan, D. J. Reducing Radiation Damage in Soft Matter with Femtosecond-Timed Single-Electron Packets. *Nano Lett.* **19**, 6687–6694 (2019).
15. Babayan, N. *et al.* Dose-rate effect of ultrashort electron beam radiation on DNA damage and repair in vitro. *J. Radiat. Res.* **58**, 894–897 (2017).
16. Kwon, O.-H., Ortalan, V. & Zewail, A. H. Macromolecular structural dynamics visualized by pulsed dose control in 4D electron microscopy. *Proc. Natl. Acad. Sci. U. S. A.* **108**, 6026–6031 (2011).
17. Kisielowski, C. *et al.* Discovering Hidden Material Properties of MgCl 2 at Atomic Resolution with Structured Temporal Electron Illumination of Picosecond Time Resolution. *Adv. Funct. Mater.* **29**, 1807818 (2019).
18. Plemmons, D. A. & Flannigan, D. J. Ultrafast electron microscopy: Instrument response from the single-electron to high bunch-charge regimes. *Chem. Phys. Lett.* **683**, 186–192

(2017).

19. Jing, C. *et al.* Tunable electron beam pulser for picoseconds stroboscopic microscopy in transmission electron microscopes. *Ultramicroscopy* **207**, 112829 (2019).
20. Qiu, J. *et al.* GHz laser-free time-resolved transmission electron microscopy: A stroboscopic high-duty-cycle method. *Ultramicroscopy* **161**, 130–136 (2016).
21. Lau, J. W. *et al.* Laser-free GHz stroboscopic transmission electron microscope: Components, system integration, and practical considerations for pump-probe measurements. *Rev. Sci. Instrum.* **91**, 021301 (2020).
22. Dorset, D. L. Electron diffraction intensities from bent molecular organic crystals. *Acta Crystallographica Section A: Crystal Physics, Diffraction, Theoretical and General Crystallography* vol. 36 592–600 (1980).
23. Egerton, R. F. Control of radiation damage in the TEM. *Ultramicroscopy* vol. 127 100–108 (2013).
24. Roberts, M. W. & Thomas, J. M. *Surface and Defect Properties of Solids*. (Royal Society of Chemistry, 2007).
25. Hayward, S. B. & Glaeser, R. M. Radiation damage of purple membrane at low temperature. *Ultramicroscopy* **04**, 201–210 (1979).
26. Unwin, P. N. & Henderson, R. Molecular structure determination by electron microscopy of unstained crystalline specimens. *J. Mol. Biol.* **94**, 425–440 (1975).
27. Henderson, R. & Unwin, P. N. Three-dimensional model of purple membrane obtained by electron microscopy. *Nature* **257**, 28–32 (1975).
28. Sonar, S. *et al.* A redirected proton pathway in the bacteriorhodopsin mutant Tyr-57-->Asp.

Evidence for proton translocation without Schiff base deprotonation. *J. Biol. Chem.* **269**, 28851–28858 (1994).

29. Baldwin, J. & Henderson, R. Measurement and evaluation of electron diffraction patterns from two-dimensional crystals. *Ultramicroscopy* **14**, 319–335 (1984).
30. Reimer, L. *Transmission Electron Microscopy: Physics of Image Formation and Microanalysis*. (Springer, 2013).
31. Leijten, Z. J. W. A., Keizer, A. D. A., de With, G. & Friedrich, H. Quantitative Analysis of Electron Beam Damage in Organic Thin Films. *J. Phys. Chem. C Nanomater. Interfaces* **121**, 10552–10561 (2017).

Acknowledgements

This work was supported by the SBIR program under NIH project number 1R43GM133267-01. The research at BNL was supported by the U.S. Department of Energy, Office of Basic Energy Sciences, Division of Materials Science and Engineering, under Contract No. DE- SC0012704. The NIST microscope was commissioned under Award No. SB1341-16-CN-0035. The authors would like to thank Dr. Michael B. Katz of NIST for his kind support and Dr. Myung-Geun Han for assistance with 200 keV JEM-2010F operation at BNL, as well as Dr. Joseph Mckeown and Dr. Megan Shelby of Lawrence Livermore National Laboratory for providing purple membrane samples and for useful discussions.